21. A. F. Moodie, C. E. Marble, *Philos. Mag.* **35**, 201 (1977).
22. G. Haas *et al.*, *Phys. Rev. B* **61**, 11105 (2000).
23. D. Kashchiev, *Thin Solid Films* **55**, 399 (1978).
24. C. L. Liu, J. M. Cohen, J. B. Adams, A. F. Voter, *Surf. Sci.* **253**, 334 (1991).
25. J.-L. Viovy, D. Beyssens, C. M. Knobler, *Phys. Rev. A* **37**, 4965 (1988).
26. D. Beyssens, C. M. Knobler, *Phys. Rev. Lett.* **57**, 1433 (1986).
27. J. Barth, H. Brune, G. Ertl, R. Behm, *Phys. Rev. B* **42**, 9307 (1990).
28. A. R. Sandy, S. G. J. Mochrie, D. M. Zehner, K. G. Huang, D. Gibbs, *Phys. Rev. B* **43**, 4667 (1991).
29. We thank all the staff of the ESRF ID32 beamline for their invaluable help during the mounting of the GISAXS setup and the measurements.

Supporting Online Material
www.sciencemag.org/cgi/content/full/300/5624/1416/DC1
Materials and Methods
Figs. S1 to S3
References and Notes
Movie S1

7 January 2003; accepted 14 April 2003

Atomic Resolution Imaging of a Carbon Nanotube from Diffraction Intensities

J. M. Zuo,[1]* I. Vartanyants,[2]† M. Gao,[1] R. Zhang,[3] L. A. Nagahara[3]

Atomic imaging of three-dimensional structures has required a crystal in diffraction or a lens in electron imaging. Whereas diffraction achieves very high resolution by averaging over many cells, imaging gives localized structural information, such as the position of a single dopant atom. However, lens aberrations limit electron imaging resolution to about 1 angstrom. Resolution is reduced further by low contrast from weak scattering or from the limitations on electron dose for radiation-sensitive molecules. We show that both high resolution and high contrast can be achieved by imaging from diffraction with a nanometer-sized coherent electron beam. The phase problem is solved by oversampling and iterative phase retrieval. We apply this technique to image a double-wall carbon nanotube at 1-angstrom resolution, revealing the structure of two tubes of different helicities. Because the only requirement for imaging is a diffraction pattern sampled below the Nyquist frequency, our technique has the potential to image nonperiodic nanostructures, including biological macromolecules, at diffraction intensity–limited resolutions.

Structure determination for crystals is currently performed with the use of x-ray and neutron diffraction, which average over many identical cells by focusing beams into directions defined by the crystal's reciprocal lattice. Local internal structures are imaged with the use of transmission electron microscopes. Resolution at ~1 Å for crystalline samples is possible with recent developments in microscopy (*1*–*3*). However, many nanostructures have not been accessible to crystallography. For example, nonperiodic nanostructures lack well-defined atomic columns and cannot be imaged in projection at current microscope resolutions. The resolution for samples that are radiation-sensitive can be further reduced by low imaging contrast from the low electron dose. In cases of biological macromolecules, atomic resolution requires an averaging of over $\geq 10^5$ molecules of the same configuration in cryoelectron microscopy (*4*).

To realize atomic resolution unlimited by microscope lens aberrations and contrast transfer functions, we used nanoarea electron diffraction (NAED) for imaging. We recorded the intensities of electron diffraction waves (or diffraction patterns) from a single double-wall carbon nanotube (DWNT) (*5*) with the use of a nanometer-sized coherent electron beam. The diffraction intensities were measured in reciprocal space at a resolution finer than the frequency of one over the sample size (the Nyquist frequency). This approach is alternatively called oversampling (*6*). Recorded intensities give only the amplitude of the diffracted wave. Direct imaging of the object requires both the amplitude and the phase of the wave function. The missing phase information is known as the phase problem. However, recent studies have shown that, in dimensions more than one, the phase problem is uniquely solvable for localized objects (*7*–*9*). The missing phase can be retrieved ab initio from diffraction intensities through an iterative procedure (*10*–*12*). We applied this approach to experimental electron diffraction patterns. The results show that this technique is capable of finding unique solutions independent of the starting phases. The approach of diffractive imaging, or imaging from diffraction intensities, appears to solve many technical difficulties in conventional imaging, namely, resolution limitations from lens aberration, sample drift, instrument instability, and low contrast in electron images.

We imaged a DWNT because of the challenge of seeing carbon and the importance of structure to its properties. The structure of a perfect carbon nanotube is a rolled-up graphene strip whose geometry is completely specified by the circumferential period, or the chiral vector, $\mathbf{c} = n\mathbf{a} + m\mathbf{b}$ ($\mathbf{a}$ and $\mathbf{b}$ are unit cell vectors of graphite, $\mathbf{a}\hat{}\mathbf{b} = 60°$, and n and m are integers) (*13*). Electron scattering by carbon is weak, and contrast in transmission electron microscopy (TEM) images has thus far been too low to see the atomic structure. Because both helical structure and carbon are common among biological single particles, DWNTs are excellent samples for testing imaging resolution and sensitivity. Also, the mechanical and electric properties of a nanotube depend on its structure (*14*). However, to date, only the outermost shell of a carbon nanotube has been imaged by scanning tunneling microscopy with atomic resolution (*15*).

To record an electron diffraction pattern from a single DWNT, we used coherent electron nanodiffraction in a JEOL (Peabody, MA) electron microscope with a field emission gun. Low-resolution electron imaging was used to locate and select the tube. Figure 1 shows the recorded electron diffraction pattern and a schematic ray diagram. The demagnified condenser aperture, rather than a focused spot (*16*), is used to limit the beam size at the sample. For an aperture 10 μm in diameter, the electron beam diameter is ~50 nm. The small probe size allows us to select a section of the tube for electron diffraction. The field emission gun provides both coherence and a high beam intensity with the probe current intensity at $\sim 10^5$ electron (e) $s^{-1}\cdot nm^2$. The electron diffraction patterns were recorded on electron imaging plates (*17*).

Information about structure is contained in the diffraction pattern recorded at far field from the sample. For carbon nanotubes, electron scattering is weak and well described by the kinematic approximation

$$I(\mathbf{k}) \propto \left| \int_{-\infty}^{\infty} \phi(\mathbf{r})[1 + i\pi\lambda U(\mathbf{r})]\exp(2\pi i\mathbf{k}\cdot\mathbf{r})d\mathbf{r} \right|^2 \quad (1)$$

Here, $U(\mathbf{r})$ equals $2m|e|V(\mathbf{r})/h^2$, with $V(\mathbf{r})$ as the Coulomb potential of the sample. The

[1]Department of Materials Science and Engineering, [2]Department of Physics, F. Seitz Materials Research Laboratory, University of Illinois at Urbana-Champaign, IL 61801, USA. [3]Physical Sciences Research Laboratories, Motorola Labs, 7700 South River Parkway, Tempe, AZ 85284, USA.

*To whom correspondence should be addressed. E-mail: jianzuo@uiuc.edu
†On leave from Institute of Crystallography Russian Academy of Science, Leninsky Prospekt. 59, 117333 Moscow, Russia.

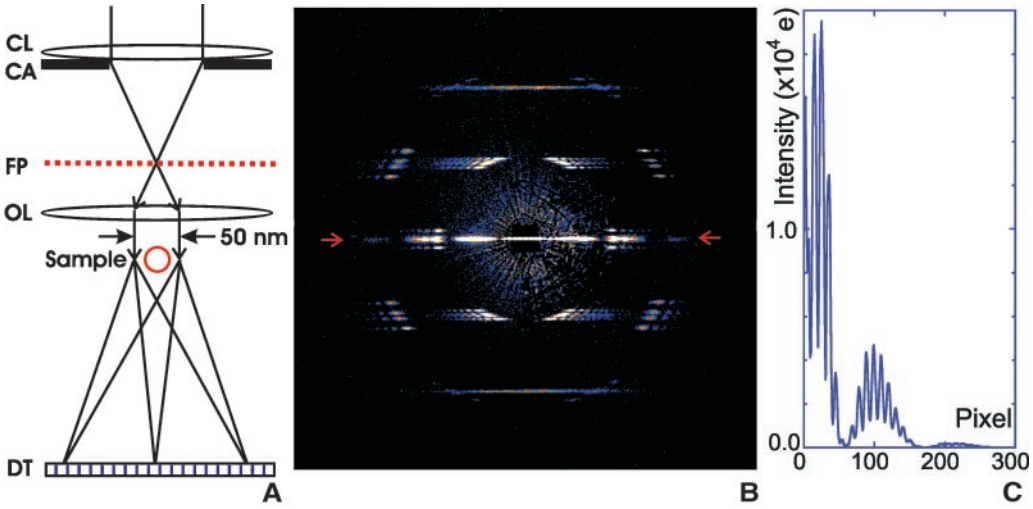

Fig. 1. Coherent nanoarea electron diffraction: (**A**) a schematic ray diagram, (**B**) the recorded diffraction pattern from a DWNT, and (**C**) the intensity profile of (B) from the center along the line indicated by arrows. The nanometer-sized parallel electron beam is formed by illuminating the condenser aperture (CA) with a coherent electron beam from the field emission electron gun and focusing the beam with the use of the condenser lens (CL) onto the front focal plane (FP) of the objective lens (OL). The size of beam is ~50 nm for a 10-μm aperture. The far-field diffraction pattern of (B) is digitized with the use of imaging plates (DT). The pixel resolution is 0.0025 $Å^{-1}$, which defines a 400 Å field of view in real space. Intensities for the center 60 pixels by 60 pixels were obtained from the Fourier transform amplitude of a low-resolution electron image of the DWNT.

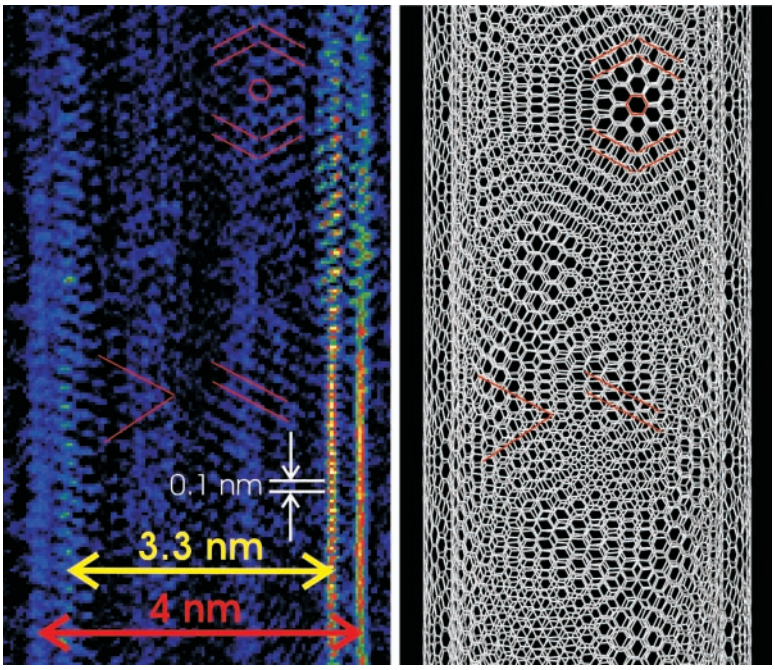

Fig. 2. (**left**) A section of the reconstructed DWNT image at 1-Å resolution and (**right**) a structural model constructed with the use of the chiral vectors of (35, 25) and (26, 24) that were determined from the image and diffraction pattern. The DWNT imaged here is one of many in our catalytic chemical vapor deposition–grown samples. Yellow and red lines mark the diameters of the inner and outer tubes, respectively. One side of walls is stronger than the other, which is because of the illumination. The DWNT is incommensurate. In projection, the structure has complex patterns showing both accidental coincidences and Moiré fringes, which are highlighted by hexagons and lines.

illuminating electron wave function $\phi(\mathbf{r})$ is formed by the electron lens. From experiments, we found that $\phi(\mathbf{r})$ has two components: a plane wave plus a weak wave packet formed by a convergent beam (*18*). Finite source size from the convergent beam and lens aberrations limit the lateral coherence of the electron beam. The finite coherence leads to a smaller field of view and a high intensity in the center of the reconstructed image (*19*). For constant illumination, the electron diffraction intensity can be expressed through the Fourier transform $F(\mathbf{k})$ of the potential $U(\mathbf{r})$ as

$$I(\mathbf{k}) \approx \delta(\mathbf{k}) + (\pi\lambda)^2 F^2(\mathbf{k}) \qquad (2)$$

For a finite nanostructure, the diffraction intensity is continuous in reciprocal space.

Both electron diffraction recording and image reconstruction are performed with discrete arrays. Experimentally, the diffraction pattern is sampled into a two-dimensional (2D) array $N \times N$ at frequency f by recording on digital imaging plates. The overall image size is $1/f$, and the size of an image pixel is $1/Nf$. We used $f = 0.0025$ $Å^{-1}$ and $N = 1024$ for a field of view of 400 Å and an image pixel size of 0.39 Å. The value of each image pixel is to be determined from the diffraction and from prior knowledge about the support. Direct image reconstruction using inverse Fourier transform requires both the amplitude and the phase. This is precluded by the missing phase in the recorded diffraction pattern. To solve the phase problem by oversampling, we illuminated an isolated DWNT, including the vacuum region surrounding the tube, and used the vacuum as support. The area ratio of the field of view (object plus the support) and object defines the oversampling ratio σ. This ratio should be larger than 2 for phase retrieval from diffraction intensities (*7*). Previously, with the use of soft x-rays of wavelength of 1.7 nm, Miao *et al*. showed that an image of patterned gold dots at a resolution of ~75 nm can be reconstructed from the diffraction pattern (*9*). For real objects, the requirement for known support is less strict than that for complex objects (*20*).

For reconstruction of the real space image, we used an iteration algorithm based on the combination of the error-reduction and hybrid input-output algorithms first proposed by Fienup (*11*). A starting image is constructed by assigning pseudorandom phases to the Fourier amplitudes from the diffraction pattern and then applying the fast Fourier transform (FFT). Iteration was carried out by back-and-forth Fourier transformation and applying constraints in real and reciprocal spaces (*21*). The calculations were then repeated with another set of starting random phases. Similar results were obtained in all cases. What is important for this approach is that it requires no guess model for the reconstruction. During iteration, the object is limited to a rectangular area of 120 pixels by 1000 pixels, and we treat area outside this box as support or vacuum. This gives an

oversampling ratio of $\sigma = S_{FFT}/S_{object} \approx 9$ (the FFT size was 1024 pixels by 1024 pixels), which is much higher than the $\sigma \geq 2$ condition required for the unique 2D reconstruction (*7*).

The reconstructed image of the double-wall carbon nanotubes from the experimental NAED pattern of Fig. 1B is shown in Fig. 2 (left). Inspection confirms that it is a double-wall tube. The fact that wall spacing is about the same on both sides provides direct support for the concentric tube model (*22*). By examining the image intensity profile, we measured the diameter of the outer wall as $D_1 = 4.04(1)$ nm; the inner wall, $D_2 = 3.33(1)$ nm; and the distance between two walls of the nanotube, $d = 0.35(1)$ nm. Most importantly, the hexagonal structure of the carbon sheet can be seen directly at localized areas. The accurate carbon nanotube diameters obtained from the image, coupled with the measurement of chiral angles from the diffraction pattern (*23*), allow a determination of the DWNT structure. The chiral vectors are (35, 25) and (26, 24) for the outer and inner tube, respectively. The two tubes are incommensurate with each other with a difference of 4.2° in helical angles. Figure 2 (right) offers a structure model for this DWNT. In projection, the overlap of four graphite layers creates Moiré fringes, which we see in our image (marked by parallel lines). There are areas of accidental coincidence where the graphite sheets align with each other. In each area, the carbon atoms are clearly resolved in the image (marked by hexagons). The carbon bond length is 1.42 Å, and features on the carbon nanotube walls are resolved with a resolution of 1 Å (*24*). All of these results support the structural model of two incommensurate, concentric, helical tubes.

We anticipate that the ability to record single-molecule diffraction with the use of NAED and the ability to reconstruct the image will find a wide range of applications in structure determinations of nonperiodic objects, from inorganic nanostructures to biological macromolecules. Because electrons interact with matter $\sim 10^4$ times more strongly than x-rays, single molecule diffraction, as we show here, can be carried out with the use of available electron sources. The resolution is diffraction intensity–limited. For radiation sensitive samples, including most biological molecules, the resolution will be limited by the amount of diffraction information that can be recorded below the radiation damage threshold. The threshold for macromolecule imaging is $\sim$ 10 e Å^{-2} (*4*). For the 50-nm-long DWNT, an electron dose of $\sim 10^3$ e Å^{-2} was needed for diffraction information at 1-Å resolution. The electron dose that a macromolecule with a large molecular weight will require will be less. Cryogenic cooling can also raise the radiation limit. Compared to the widely used phase-contrast imaging for biological samples, diffraction patterns record high-frequency structural information that is not limited by lens aberration and that has a large signal-to-noise ratio for structures with a high degree of order, such as carbon nanotubes. Both are favorable factors for the use of NAED for high-resolution imaging (*25*).

References and Notes

1. J. C. H. Spence, *Science* **299**, 839 (2003).
2. C. L. Jia, M. Lentzen, K. Urban, *Science* **299**, 870 (2003).
3. M. A. O'Keefe *et al*., *Ultramicroscopy* **89**, 215 (2001).
4. R. Henderson, *Q. Rev. Biophys*. **28**, 171 (1995).
5. DWNT synthesis and observation are described on *Science* Online.
6. D. Sayre, *Acta Crystallogr. A* **5**, 843 (1952).
7. R. Bates, *Optik* **61**, 247 (1982).
8. R. P. Millane, *J. Opt. Soc. Am. A* **7**, 394 (1990).
9. J. Miao, P. Charalambous, J. Kirz, D. Sayre, *Nature* **15**, 342 (1999).
10. R. W. Gerchberg, W. O. Saxton, *Optik* **35**, 237 (1972).
11. J. Fienup, *Appl. Opt*. **21**, 2758 (1982).
12. R. P. Millane, W. J. Stroud, *J. Opt. Soc. Am. A* **14**, 568 (1997).
13. S. Iijima, *Nature* **354**, 56 (1991).
14. A. Jorio *et al*., *Phys. Rev. Lett*. **86**, 1118 (2001).
15. C. Dekker, *Phys. Today* **52**, 22 (1999).
16. J. Miao *et al*., *Phys. Rev. Lett*. 89, 155502 (2002). A focused electron beam was proposed for oversampling the electron diffraction pattern in the reported computational experiment. The beam convergence then limits the smallest sampling frequency.
17. The original pattern has a strong central peak and background from aperture scattering. We removed them by subtracting a diffraction pattern recorded without the tube. This results in an area of 60 pixels by 60 pixels with missing intensity. To fill this gap, we use the amplitude of Fourier transform of a low-resolution electron image.
18. The illuminating electron wave has the form of

$$\phi(\mathbf{r}) = \int_{-\infty}^{\infty} A(\mathbf{k}_\parallel) \exp\left[i\pi k_\parallel^2 \lambda \left(\frac{C_s \lambda^2}{2} k_\parallel^2 + \Delta f \right) \right] \exp(2\pi i \mathbf{k}\cdot\mathbf{r}) d\mathbf{k}_\parallel$$

Here, C_s and Δf are the spherical aberration and the defocus of the electron lens, respectively. $A(\mathbf{k}_\parallel)$ has two components, a sharp peak on a broad background. Both can be modeled as a Gaussian function. The Gaussian half width of the sharp peak is $\sim$ 0.05 mrad, which can be approximated as a plane wave illumination.
19. I. A. Vartanyants, I. K. Robinson, *J. Phys. Condens. Matter* **13**, 10593 (2001).
20. J. C. H. Spence, U. Weierstall, M. Howells, *Philos. Trans. R. Soc. London Ser. A* **360**, 875 (2002).
21. We used the following constraints: In reciprocal space, the calculated amplitude on each iteration step was replaced by the measured Fourier amplitude $(I_{exp})^{1/2}$, keeping the phases. After the first $\sim$50 iterations, the central part of the diffraction pattern (60 pixels by 60 pixels) was allowed to vary without any constraint (only the high-resolution diffraction image was then used in these steps). In real space, the most important constraints for reconstruction of the electron interaction potential $U(\mathbf{r})$ are that the image has to be real and positive. We used the R factor defined by $R = \Sigma \| F^{exp} \| - | F^{Fit} | / \Sigma | F^{exp} |$ to monitor the convergence of phase retrieval iterations. The best fit was selected from images with the lowest R.
22. In the image, one side of the DWNT is much sharper than the other. This effect comes partly from the variations in the projected potential along the wall and partly from an effect we attribute to a nonuniform illumination in the TEM.
23. M. Gao *et al*., *Appl. Phys. Lett*. **82**, 2703 (2003).
24. The nominal microscope point resolution is 2.2 Å for normal imaging at the Scherzer focus conditions, with C_s = 1 mm and wavelength of 0.025 Å for the JEOL2010F microscope operated at 200 kV.

25. Work on electron microscopy characterization was supported by DOE DEFG02-01ER45923 and DEFG02-91ER45439 and the TEM facility of Center for Microanalysis of Materials at the Frederick Seitz Materials Research Laboratory. We thank J. H. Weaver, I. Robinson, S. Granick, R. Twesten, I. Petrov, R. Tsui, and H. Goronkin for discussion and encouragement.

Supporting Online Material

www.sciencemag.org/cgi/content/full/300/5624/1419/DC1
Materials and Methods
SOM Text
Fig. S1

26 February 2003; accepted 16 April 2003

Using 1-Hz GPS Data to Measure Deformations Caused by the Denali Fault Earthquake

Kristine M. Larson,[1]* Paul Bodin,[2] Joan Gomberg[3]

The 3 November 2002 moment magnitude 7.9 Denali fault earthquake generated large, permanent surface displacements in Alaska and large-amplitude surface waves throughout western North America. We find good agreement between strong ground-motion records integrated to displacement and 1-hertz Global Positioning System (GPS) position estimates collected $\sim$140 kilometers from the earthquake epicenter. One-hertz GPS receivers also detected seismic surface waves 750 to 3800 kilometers from the epicenter, whereas these waves saturated many of the seismic instruments in the same region. High-frequency GPS increases the dynamic range and frequency bandwidth of ground-motion observations, providing another tool for studying earthquake processes.

Our understanding of how faults rupture during major earthquakes is limited by our observational capabilities; they also limit our understanding of the resulting ground deformation. Within a distance range of about the same dimension as the fault rupture (the near field), the surface deformation pattern is composed of a highly spatially variable permanent strain field generated by permanent displacements across the fault surface (coseismic offsets). These displacements form within tens of seconds and are superimposed on transient defor-